

A fast Visible-Infrared Imaging Radiometer Suite simulator for cloudy atmospheres

Chao Liu¹, Ping Yang^{1,*}, Shaima L. Nasiri¹,

Steven Platnick², Kerry G. Meyer^{3,2}, Chenxi Wang⁴, Shouguo Ding⁵

1. Department of Atmospheric Sciences, Texas A&M University, College Station,
TX 77843

2. NASA Goddard Space Flight Center, Greenbelt, MD, 20771

3. Goddard Earth Sciences Technology and Research, Universities Space Research
Association, Columbia, MD 21044

4. Earth System Science Interdisciplinary Center, University of Maryland, College
Park, MD 20740

5. Department of Earth and Atmospheric Sciences, University of Nebraska-
Lincoln, Lincoln, NE 68588

Submitted to

Journal of Geophysical Research – Atmosphere

Corresponding author address: Prof. Ping Yang, Department of Atmospheric Sciences,
Texas A&M University, College Station, TX 77843, USA; Email: pyang@tamu.edu

Key Points:

- Correlated k -distribution models for the VIIRS bands are developed
- A fast VIIRS instrument simulator is developed
- A case study is performed to validate the simulator

Abstract

A fast instrument simulator is developed to simulate the observations made in cloudy atmospheres by the Visible Infrared Imaging Radiometer Suite (VIIRS). The correlated k -distribution (CKD) technique is used to compute the transmissivity of absorbing atmospheric gases. The bulk scattering properties of ice clouds used in this study are based on the ice model used for the MODIS Collection 6 ice cloud products. Two fast radiative transfer models based on pre-computed ice cloud look-up-tables are used for the VIIRS solar and infrared channels. The accuracy and efficiency of the fast simulator are quantified in comparison with a combination of the rigorous line-by-line (LBLRTM) and discrete ordinate radiative transfer (DISORT) models. Relative errors are less than 2% for simulated TOA reflectances for the solar channels and the brightness temperature differences for the infrared channels are less than 0.2 K. The simulator is over three orders of magnitude faster than the benchmark LBLRTM+DISORT model. Furthermore, the cloudy atmosphere reflectances and brightness temperatures from the fast VIIRS simulator compare favorably with those from VIIRS observations.

47

48 **1. Introduction**

49 The Visible Infrared Imaging Radiometer Suite (VIIRS) on board the Suomi National
50 Polar-orbiting Partnership (Suomi NPP) satellite provides critical data for accurately
51 determining cloud and aerosol properties, ocean color, sea and land surface temperatures,
52 ice motion and temperature, fires, and Earth's albedo [Lewis et al., 2010; Lee et al., 2010;
53 Hillger et al., 2013]. VIIRS includes 16 moderate-resolution channels (referred to as M-
54 bands) at 0.75-km spatial resolution and 5 higher-resolution imagery channels (I-bands) at
55 0.375-km resolution. With central wavelengths from approximately 0.4 to 12 μm , the
56 sensor was designed to be the next-generation global weather and climate imager for
57 afternoon polar orbiting observations. To infer cloud properties from the VIIRS
58 observations, an accurate and efficient forward radiative transfer model (RTM) is
59 invaluable for generating simulated reflectances or brightness temperatures for a variety of
60 atmospheric cloud and surface conditions, and can be used for retrieval error analyses and
61 instrument calibration efforts.

62 Many rigorous radiative transfer schemes, such as the line-by-line radiative transfer
63 model (LBLRTM) [Clough et al., 1992, 2005], the adding-doubling (AD) algorithm
64 [Twomey et al., 1966; Hovenier, 1969; Hansen, 1971; de Haan et al., 1987], and the
65 discrete ordinates radiative transfer (DISORT) method [Chandrasekhar, 1960; Liou, 1973;
66 Stamnes et al., 1988; Thomas and Stamnes, 1999], have been developed and widely applied
67 under different circumstances. For remote sensing problems involving hyperspectrally
68 resolved or channel-averaged radiances, a rigorous approach is needed to independently
69 and efficiently perform large numbers of simulations for each wavelength/wavenumber

70 due to the significant spectral variations exhibited by molecular absorption, and, in the case
71 of channel-averaged simulation, to conduct subsequent spectral integration. Performing
72 hundreds or even thousands of monochromatic simulations is extremely time-consuming;
73 thus, rigorous RTMs are significantly limited in satellite remote sensing applications
74 because of the large number of spatial and temporal observations. Developing
75 computationally efficient RTMs for specific satellite-based instruments is critical for
76 operational retrievals of atmospheric profiles as well as for the advancement of more
77 sophisticated cloud or aerosol property retrievals [Dubuisson et al., 1996, 2005; Weisz,
78 2007; Garnier et al., 2012, 2013; Chen and Huang, 2014].

79 One approach to achieve computational efficiency is to relax the accuracy constraints
80 for each individual simulation; models using two streams [Meador and Weaver, 1980], low
81 orders of scatterings [Natraj and Spurr, 2007], or pre-computed look-up-tables [Wang et
82 al., 2012] are typical examples of such approximations. These models normally keep the
83 same number of single simulations, but accelerate each individual simulation. Other
84 approximate approaches for hyperspectral or band-average calculations such as the
85 correlated k-distribution (CKD) method [Arking and Grossman, 1972; Lacis and Oinas,
86 1991; Fu and Liou, 1992; Kratz, 1995; Shi et al., 2009], the principal component method
87 [Liu et al., 2006, 2009], and the optimal spectral sampling method [Moncet et al., 2008],
88 are designed to minimize the computational effort by reducing the number of individual
89 radiative transfer simulations within a spectral band. Instead of considering each
90 wavenumber within a band, such models conduct rigorous radiative transfer calculations
91 at only a small number of representative monochromatic wavenumbers. The two types of
92 approaches have been applied to remote sensing, radiative transfer, and GCMs in both the

solar and IR spectral regions. In this study, we combine the two approaches to maximize computational efficiency.

This study develops a fast RTM, i.e., an instrument simulator for cloudy atmospheres, and uses both of the previously described methodologies to minimize the computational time. While the emphasis here is in simulating the VIIRS solar and infrared channels, the approach can be easily extended to other imagers. To obtain top-of-atmosphere (TOA) reflectances or brightness temperatures, the atmospheric gaseous transmissivity and cloud optical properties are essential parameters for a RTM, and will be carefully considered in the fast model. Section 2 describes the development of the CKD models to determine gaseous transmissivity, and Section 3 discusses the cloud optical properties. The fast radiative transfer models (FRTMs) for VIIRS solar and IR channels, respectively, are described in Section 4. Section 5 validates the simulator and compares the simulated results with VIIRS observations, and Section 6 summarizes the study.

2. Determination of gas transmissivity

As an approximate technique to line-by-line calculations such as those of LBLRTM [Clough et al., 1992, 2005], the CKD is a highly efficient model to account for gaseous absorption, and can be easily incorporated into calculations of multiple scattering in aerosols and clouds. The CKD model replaces the integral of gas transmissivity over highly variable spectral space by one over a much smoother absorption coefficient space.

The transmissivity of a single gas at constant pressure and temperature within a small spectral interval of interest, e.g., the interval of a VIIRS channel, is defined as:

$$T_{ch}(u) = \frac{1}{\Delta v} \int_{\Delta v} e^{-k(v)u} dv , \quad (1)$$

where $k(v)$ is the gas spectral absorption coefficient at wavenumber v , and u is the gas path-length. To accurately obtain the transmissivity, the line-by-line calculation must be performed over a very fine wavenumber grid. This calculation requires significant computational time because the absorption coefficient is a highly variable function in spectral space. However, the transmissivity does not depend on the ordering of the spectral absorption coefficient within a given spectral interval, and, thus, instead of integrating over the spectral space, Eq. (1) can be expressed as:

$$T_{ch}(u) = \frac{1}{\Delta v} \int_{\Delta v} e^{-k(v)u} dv = \int_{k_{min}}^{k_{max}} e^{-ku} f(k) dk, \quad (2)$$

where $f(k)$ is the normalized probability distribution function for $k(v)$. To obtain $f(k)$, the range of the absorption coefficient $k(v)$ ($[k_{min}, k_{max}]$) and the spectral interval are divided into N and M uniform subintervals, respectively, with width $\delta k = \frac{k_{max}-k_{min}}{N}$, and $\delta v = \frac{\Delta v}{M}$. We define $k_0 = k_{min}$, $k_n = k_{n-1} + \delta k$, and $v_m = (m - 0.5)\delta v$. Thus, the probability function $f(k)$ can be numerically represented by:

$$f(k_i) = \frac{1}{\Delta v} \sum_{m=1}^M \frac{\delta v}{\delta k} W(k_{i-1} < k(v_m) \leq k_i), \quad (3)$$

where W is the weighting function equal to unity if its argument condition is satisfied and zero otherwise. By defining the cumulative probability function $g(k) = \int_{k_{min}}^k f(k') dk'$, or in the discrete format,

$$g(k_i) = \frac{1}{\Delta v} \sum_{m=1}^M \delta v W(k(v_m) \leq k_i) = \sum_{j=1}^i f(k_j) \delta k, \quad (4)$$

Eq. (1) can be further simplified as:

$$T_{ch}(u) = \int_0^1 e^{-k(g)u} dg, \quad (5)$$

where g ranges from 0 to 1, and $k(g)$ is a monotonically increasing and smooth function of g . Thus, the spectral integration in Eq. (5) can be evaluated with fewer points in g space

between zero and unity compared to the number of wavenumber points required for Eq. (1). This approximation is known as the k -distribution method and can be given by:

$$T_{ch}(u) = \int_0^1 e^{-k(g)u} dg = \sum_{i=1}^P e^{-k(g_i)u} \Delta g_i. \quad (6)$$

To extend the k -distribution method to realistic inhomogeneous atmospheres, the CKD method assumes that the ordering of absorption lines with respect to their strengths is the same at different temperature and pressure levels, and

$$\begin{aligned} T_{ch}(u) &= \frac{1}{\Delta v} \int_{\Delta v} \exp \left[- \int_{z_1}^{z_2} k(v, P(z), T(z)) \rho dz \right] dv \\ &= \int_0^1 \exp \left[- \int_{z_1}^{z_2} k(g, P(z), T(z)) \rho dz \right] dg \end{aligned} \quad (7)$$

where $P(z)$ and $T(z)$ are the pressure and temperature of the atmospheric layer between z_1 and z_2 .

While the CKD method has been widely used, the spectral k 's from multiple gases have typically been treated as uncorrelated so that a product rule approximation could be used. Edwards and Francis [2000] suggested an approach to treat overlapping lines from different gases as a “single gas” by combining the absorption coefficients of multiple absorption gases. The equivalent absorption coefficient for a given mixture of $(N+1)$ gases is defined as:

$$K(v, R_1, R_2, \dots, R_N) = k_0(v) + \sum_{i=1}^N k_i(v) R_i, \quad (8)$$

where $k_i(v)$ is the absorption coefficient of the i th gas, and R_i is the density ratio of the i th gas to the reference gas, i.e., the gas with absorption coefficient of $k_0(v)$. The dominant gas can be regarded as the reference gas, and, through Eq. (8), the absorption of $(N+1)$ gases is converted into a single-gas case with equivalent absorption coefficient $K(v, R_1, R_2, \dots, R_N)$. This process can be repeated for a finite number of gas mixture density

ratios for a fixed set of constituent gases, such that $K(v)$ for any given mixture of these gases can be found by interpolation.

To consider an instrument channel's (i.e., VIIRS) spectral response function (SRF, i.e. $s(v)$), the spectral transmissivity given by Eq. (1) is rewritten as:

$$T_{ch}(u) = \frac{1}{S} \int_{\Delta v} s(v) e^{-k(v)u} dv, \quad (9)$$

where the normalization factor is $S = \int_{\Delta v} s(v) dv$. To include the SRF in the CKD model, the approach given by Edwards and Francis [2000] is used, and Eqs. (3) and (4) are modified as:

$$f_s(k_i) = \frac{1}{S} \sum_{m=1}^M \frac{s(v_m) \delta v}{\delta k} W(k_{i-1} < k(v_m) \leq k_i), \quad (10)$$

and

$$g_s(k_i) = \frac{1}{S} \sum_{m=1}^M s(v_m) \delta v W(k(v_m) \leq k_i) = \sum_{j=1}^i f_s(k_j) \delta k. \quad (11)$$

In Eqs. (10) and (11), the uniform weighting δv is changed into $s(v_m) \delta v$ for each spectral subinterval. TOA solar spectral irradiance variations in the channel can also be included in the normalization factor in a manner similar to the SRFs.

Fig. 1 illustrates the treatments of overlapping absorption lines, SRF, and solar spectral irradiance for the VIIRS M10 channel centered at a wavelength of 1.61 μm . The gas spectral absorption coefficients of CO_2 , H_2O , and CH_4 are plotted in (a), (b), and (c), respectively, with (d) showing the effective absorption coefficient of a mixture with mass density ratios of H_2O and CH_4 to CO_2 of 0.1 and 0.001, respectively. Following Eqs. (10) and (11), the effective coefficient of the mixture gas is weighted with the corresponding SRF (e) and solar spectral irradiance (SI) (f). Fig. 1(g) shows the sorted effective absorption

coefficient as a function of g (blue line); results without considering either the SRF or solar spectral irradiance is illustrated for comparison (red line). In g space, the absorption coefficient becomes a smooth function, and only 4 intervals (shown by the dashed lines in (g)) in this channel are used to determine the transmissivity following Eq. (6). Furthermore, differences are obvious for results with and without consideration of the SRF, as shown in Fig. 1g.

Based on the theories and techniques described, we construct a CKD model for each of the VIIRS channels, considering only up to the three most absorptive gases. The parameters used to construct the CKD models follow the work done by Ding et al. [2012] for the Geostationary Operational Environmental Satellite R (GEOS-R) Advanced Baseline Imager (ABI) solar channels. To build the CKD model for each of the VIIRS channels, the absorption coefficients of the gases of interest are obtained from the LBLRTM, and the molecular absorption line parameters are based on the 2008 edition of the High Resolution Transmission (HITRAN) molecular spectroscopic database [Rothman et al., 2008]. The absorption coefficients are calculated at 19 pressure levels and 3 temperatures (i.e., 200K, 260K, and 320K) using the LBLRTM, and each set of absorption coefficients are sorted and binned following the same distribution as that of the reference pressure and temperature, chosen as 261 hPa and 260 K, respectively. Each of the VIIRS channels is divided into 4 to 16 intervals in g -space, the number of which is determined by the degree of the gas absorption and the complexity of the overlapping gaseous absorption.

At a given g and pressure level P_o , the absorption coefficient at temperature T is given by:

$$\ln[k(g, P_o, T)] = a(g, P_o) + b(g, P_o)(T - 260) + c(g, P_o)(T - 260)^2, \quad (12)$$

where the coefficients a , b and c are regression coefficients derived from absorption coefficients obtained at the three temperature values of 200 K, 260 K, and 320 K for the corresponding g values at the 19 pressure levels. In practice, the absorption coefficient at an arbitrary temperature and pressure, $k(g, P, T)$, is found first by solving Eq. (12) first, then by linear interpolation between values at the two neighboring pressures.

Table 1 lists parameters of the CKD model for each VIIRS channel, including the central wavelength, wavelength range, absorbing gas species considered, and the number of g values. Gases considered in this study include H₂O, O₂, O₃, CO₂, CH₄, and N₂O. Up to three different absorbers are considered for each channel, and the O₃ continuum absorption (designated as “cont.” in the table) is included in the IR channels by using the equations given by Roberts et al. [1976].

The CKD is employed to produce the transmissivity of the atmosphere, and Fig. 2 compares the band-averaged transmissivity and weighting profiles with results from the LBLRTM to illustrate the accuracy of the model for clear sky calculations. Results for four VIIRS channels centered at wavelengths 0.555 μm , 1.61 μm , 3.7 μm , and 10.763 μm , are shown. In the simulations, the US standard atmospheric profile is divided into 50 layers, each being 1 km thick, and the volume mixing ratios of O₂, CO₂, CH₄, and N₂O are assumed to be uniform with values of 0.21, 3.8×10^{-4} , 1.8×10^{-6} , and 3.2×10^{-7} . From left to right in Fig 2, the three columns correspond to the transmissivity in each layer, relative transmissivity error, and weighting function profiles of the CKD models. Fig. 2 indicates that the relative errors in transmissivity are less than 0.1% for the four VIIRS channels, which, from a practical application perspective, are sufficiently accurate for simulating TOA reflectance and brightness temperatures under cloudy conditions.

226

227 **3. Determination of cloud optical properties**

228 For cloudy sky applications, channel-averaged cloud bulk-scattering properties, for
229 both liquid and ice phases, are required to determine the absorption, scattering, and
230 emission of cloud layers. Here, single-scattering calculations are performed at discrete
231 sizes and wavelengths, and averaged over the assumed particle size distribution and the
232 SRF for each VIIRS channel. For the solar channels, the solar spectral irradiance is also
233 considered. For the IR bands, the Planck function representing the thermal IR emission
234 from an opaque cloud at 233 K is used. The details for obtaining the channel-averaged
235 properties can be found in Baum et al. [2005].

236 For liquid phase clouds, the single-scattering properties are obtained using the Lorenz-
237 Mie theory [Mie, 1908]. The cloud droplet size distributions are assumed to be Gamma
238 distributions [Hansen and Travis, 1974] with an effective variance of 0.1, and the bulk-
239 scattering properties are calculated for effective radii ranging from 2 to 50 μm .

240 For ice phase clouds the model choice is critical, because the microphysical and optical
241 properties of ice clouds are very sensitive to particle habits, especially the optical properties
242 in solar reflectance channels. The ice cloud model used for deriving the MODIS Collection
243 6 cloud products is applied in this study. This model consists of a single ice habit, i.e., a
244 severely roughened aggregate with eight solid hexagonal columns, that provides excellent
245 spectral consistency (i.e., between optical thicknesses inferred from solar reflectance and
246 IR channels) and close agreement with the polarization properties from the PARASOL
247 observations [Baum et al. 2014]. The column aggregate single-scattering properties are
248 obtained from the ice crystal database developed by Yang et al. [2013]. The Gamma size

distribution with an effective variance of 0.1 is assumed for the ice clouds, and the effective diameter ranges from 10 to 180 μm in 10 μm steps.

4. VIIRS simulator

This study considers both the VIIRS solar reflectance and infrared channels. For solar channels, cloud multiple scattering plays a much more significant role than the gaseous absorption and emission, because absorption is relatively weak at most VIIRS solar channels (except the M9 channel with strong water vapor absorption), and emissions at these wavelengths are negligible. However, gaseous absorption and emission become as important as cloud and aerosol effects (scattering, absorption, and emission) in the infrared channels. Thus, the VIIRS solar and infrared channels use different fast radiative transfer models (FRTMs).

The FRTM developed by Wang et al. [2013a] is chosen to calculate visible through shortwave infrared spectral reflectance. This FRTM uses six independent radiative transfer equations to approximate the full radiative transfer processes for a combination of cloud, aerosol, or molecular layers; the adding-doubling algorithm implemented on a twisted icosahedral mesh is incorporated to account for overlapped cloud/aerosol layers. To further improve the FRTM efficiency, the bidirectional reflectance and transmittance distribution functions (BRDF and BTDF) of cloud layers with different optical thicknesses and effective particle sizes are pre-calculated using the 128-stream DISORT, and the optical properties of water and ice clouds, discussed in the previous section, are included. Generally, the FRTM is approximately two orders of magnitude faster than the 128-stream DISORT, and obtains TOA reflectance with relative errors normally less than 5%.

For the infrared channels, the simulator uses the FRTM developed by Wang et al. [2011, 2013b] to obtain the TOA brightness temperature. Similar to the FRTM used for the solar channels, the effects of cloud layers are efficiently considered by pre-calculated look-up-tables at various optical thicknesses and effective particle sizes, which include the reflectance, transmittance, emissivity, and effective temperature. The CKD model discussed in Section 2 is used to account for atmospheric gas absorption. The TOA brightness temperature differences (BTDs) given by the fast model and the rigorous DISORT are less than 0.15 K. Furthermore, the FRTM is more than three orders of magnitude faster than the corresponding a DISORT implementation with 32 streams.

The most current DISORT code (DISORT 2.0 beta) is used to calculate the look-up-tables for both FRTMS based on the band-averaged optical properties. In DISORT, the cloud phase functions are defined in terms of their Legendre polynomial expansion coefficients and, for large ice particles, thousands of Legendre polynomial terms are needed to represent a phase function that has a strong forward peak. The number of expansion terms can be greatly reduced, however, by truncating the forward peak of the phase function. The δ -fit method [Hu et al., 2000] is used here for the solar channels, such that only 128 terms are sufficient to reconstruct the phase function, significantly decreasing computational time in the DISORT simulations. Corresponding scaling adjustments are made to the optical thickness and single-scattering albedo to account for the truncated forward energy.

The solar and IR FRTMs are combined with the CKD method to maximize the efficiency of the simulator. For each simulation, the FRTM is performed with the

transmissivity obtained under each g value, and the TOA radiance of a given channel is obtained by:

$$I_{ch,simulator} = \sum_{i=1}^M I[T(g_i)]\Delta g_i, \quad (13)$$

where $T(g_i)$ refers to the transmissivity of the i th g value, and $I[T(g_i)]$ is the corresponding TOA radiance given by the FRTM.

The accuracy and efficiency of the simulator, i.e., the model based on the combination of the CKD and FRTMs, are evaluated by comparing the simulated band-averaged reflectance or BT at the TOA with the rigorous solutions given by the combination of the LBLRTM and DISORT. The spectral resolution of the LBLRTM+DISORT simulation is chosen to be 1.0 and 0.1 cm^{-1} for the solar and infrared channels, respectively, and the TOA upwelling radiances are then averaged over the spectrum considering the SRF:

$$I_{ch,std} = \frac{\int_{\Delta\nu} s(\nu)I(\nu)d\nu}{S}, \quad (14)$$

where $I(\nu)$ is the radiation at wavenumber ν given by the DISORT. With the TOA radiance, obtaining the corresponding reflectivity and brightness temperature is straightforward.

A set of comparisons at solar channels is implemented between the fast simulator and the rigorous approach, with the relative errors of TOA reflectance as a function of the viewing zenith angle shown in Fig. 3. Three VIIRS channels (M4, M10, and M11) are considered for the comparison, and three solar zenith angles values (10° , 30° and 50°) are used. The left panels are for an optical thickness of 5, and the right panels are for a value of 20. For all cases, the simulator yields relative errors less than 1.5% with respect to the

rigorous approach. The relative errors slightly increase as the solar zenith angle increases, and show little dependence on the cloud optical thickness.

To validate the simulator at the IR channels, Fig. 4 illustrates the brightness temperature differences (BTDs) given by the simulator and the LBLRTM+DISORT at three IR channels (M14, M15, and M16). The BTD is defined as:

$$\text{BTD} = \text{BT}_{\text{Simulator}} - \text{BT}_{\text{LBLRTM+DISORT}}. \quad (15)$$

Each panel of Fig. 4 shows the comparison of simulation results based on a surface emissivity of 1 and viewing zenith angle of 20° under different cloud conditions. The BTD is expressed as a function of optical thickness, and cloud particle effective diameters and top temperatures used for the simulations are listed in the figure. The errors in the BTDs are smaller than 0.2 K and decrease to less than 0.1 K for optically thick clouds.

5. Comparison with VIIRS observations

We developed a fast radiance simulator to calculate TOA reflectances or brightness temperatures of a cloudy atmosphere based on a combination of the CKD and FRTMs for the VIIRS solar and infrared channels. This section highlights a case study to assess the performance of the simulator by comparing simulated TOA reflectances and brightness temperatures with those from VIIRS observations.

As discussed in the previous sections, the forward model requires atmospheric profiles and cloud properties as input parameters. For this comparison, atmospheric profile data is obtained from the Modern Era Retrospective-analysis for Research and Applications (MERRA) [Rienecker et al., 2008] instantaneous 3-hour vertical atmospheric profile product (i.e., inst3_3d_asm_Cp) that provides temperature, geopotential height, water

vapor, and ozone concentrations at 42 pressure levels on a 288×144 mesh grid with a $1.25^\circ \times 1.25^\circ$ resolution. The cloud input to the simulator, including cloud thermodynamic phase, top pressure, optical thickness, and effective particle size, is from the operational MODIS Collection 6 cloud products (i.e., the Aqua MODIS MYD06_L2 product), and the 1 km-resolution geolocation is obtained from the MYD03 dataset. The atmospheric profiles and cloud properties are collocated with the VIIRS observations, with VIIRS solar and sensor view geometries used as simulator inputs.

A flowchart summarizing the fast VIIRS radiance simulator process is shown in Fig. 5. The atmospheric profile is input into the CKD models to generate transmissivity of absorption gases, and also provides the temperature profile for the IR simulator. The gaseous transmissivity and cloud properties are used by the FRTMs to calculate reflectances or brightness temperatures of given VIIRS solar-satellite geometries, and the simulated results are compared with the corresponding VIIRS measurements to assess the performance of the simulator.

To avoid uncertainties associated with satellite-based cloud retrievals due to larger surface reflectances over land, only observations over ocean are considered for the present case study, specifically, the VIIRS granules taken over the South Pacific Ocean from 00:38:47.4 to 00:41:38.2 UTC on 3 January 2014. The collocated MODIS granule is taken at 00:45 UTC, approximately 4 to 6 minutes behind the VIIRS observations. Fig. 6 shows the true color images of the (a) MODIS and (b) VIIRS granules, with the MODIS cloud optical thickness and effective particle radius shown in (c) and (d), respectively. The red boxes in the RGBs show the region of the simulation, which is largely covered by ice

clouds. In the simulation region, the cloud optical thickness ranges from a few to over 50, and the effective particle radius shows values from 5 to approximately 40 μm .

Fig. 7 compares the observed (left panels) and simulated (right panels) reflectances at VIIRS 0.86- and 2.25- μm channels (M7 and M11). The reflectance values at the 0.86- μm channel are larger than those at the 2.25- μm channel, which is mainly due to the significant differences in the scattering properties of ice clouds at the two channels (e.g., ice clouds are much more absorptive at the 2.25- μm channel). The patterns of the reflectances given by the fast simulator are almost the same as the VIIRS observations at each channel. Furthermore, the agreement indicates the performance of the MOD06 product that is used as the input parameters. However, note that the liquid water and ice cloud radiative models used in the FRTM were specifically chosen to match the models used in MYD06_L2 (see Sect. 3).

Fig. 8 is the same as Fig. 7 but for brightness temperatures at three VIIRS IR channels (i.e., 8.55-, 10.76-, and 12.01- μm channels (M14, M15, and M16) from upper to lower panels). The simulated brightness temperatures show close agreement with the observations. However, noticeable differences exist in some regions of the granules, and this may be due to the uncertainties in either atmospheric profiles or cloud height. The ice cloud properties, which are retrieved from MODIS solar-channel observations, may also yield significant errors when applied to IR channels, because the cloud optical thickness and effective particle radius inferred from the solar and IR channels can be quite different [Baum et al., 2014]. The case study indicates the exceptional performance of the VIIRS simulator for both solar and IR channels.

6. Summary

This study developed a computationally efficient simulator for the VIIRS solar and IR channels in cloudy atmospheres that can be used in cloud property evaluations and retrievals. The absorption of atmospheric gases and overlapping gas absorption is accounted for using a VIIRS-specific CKD that considers both the spectral response function and solar spectral irradiance. The accuracy of the transmissivity profile is estimated by comparing with the exact line-by-line results, and the relative errors in transmissivity are less than 0.1% for all VIIRS channels. Two fast RTMs are used to consider absorption, scattering, and emission of cloud layers. The channel-averaged bulk-scattering properties of roughened hexagonal columns are used for ice cloud, and the properties of water cloud are given by the Lorenz-Mie theory. By comparing with the rigorous DISORT results, the relative errors for TOA reflectance at VIIRS solar channels are less than 1.5%, and the differences in brightness temperatures at the IR channels are less than 0.25K. The present simulator is more computationally efficient than the standard LBLRTM+DISORT by over three orders of magnitude. With collocated MERRA atmospheric profiles and cloud optical thickness and effective particle diameter from the MODIS cloud product as input, the reflectances and brightness temperatures calculated by the fast simulator show close agreement with concurrent VIIRS solar and IR observations. Considering the accuracy and efficiency provided, the simulator can be used directly for cloud property retrievals related to VIIRS observations. While our fast radiative transfer model (FRTM) used in this study was applied to VIIRS channels, the FRTM can also be developed for MODIS and other satellite or airborne imagers with similar spectral coverage.

406

407 **Acknowledgement**

408 The research was supported by the NASA Grant NNX11A055G and partly by the
409 endowment funds related to the David Bullock Harris Chair in Geosciences at the
410 College of Geosciences, Texas A&M University. All computations were carried out at the
411 Texas A&M University Supercomputing Facility.

412

References

- Arking, A., and K. Grossman (1972): The influence of line shape and band structure on temperatures in planetary atmospheres, *J. Atmos. Sci.*, 29, 937-949.
- Baum, B. A., P. Yang, A. J. Heymsfield, S. Platnick, M. D. King, and S. M. Thomas (2005): Bulk scattering properties for the remote sensing of ice clouds II: narrowband models, *J. Appl. Meteor.*, 44, 1896-1911.
- Baum, B. A., P. Yang, A. J. Heymsfield, A. Bansemer, B. H. Cole, A. Merrelli, C. Schmitt, and C. Wang (2014), Ice cloud single-scattering property models with the full phase matrix at wavelengths from 0.2 to 100 μm , *J. Quant. Spectrosc. Radiat. Transfer*, 146, 123-139.
- Chandrasekar, S. (1960), *Radiative Transfer*, Dover, New York.
- Chen, X., and X. Huang (2014), Usage of differential absorption method in the thermal IR: A case study of quick estimate of clear-sky column water vapor, *J. Quant. Spectrosc. Radiat. Transfer*, 140, 99-106.
- Clough, S. A., M. J. Iacono, and J. L. Moncet (1992), Line-by-line calculation of atmospheric fluxes and cooling rates: Application to water vapor, *J. Geophys. Res.*, 97(D14), 15761-15785, doi:10.1029/92JD01419.
- Clough, S. A., M. W. Shephard, E. J. Mlawer, J. S. Delamere, M. J. Iacono, K. Cady-Pereira, S. Boukabara, and P. D. Brown (2005), Atmospheric radiative transfer modeling: a summary of the AER codes, Short Communication, *J. Quant. Spectrosc. Radiat. Transfer*, 91, 233-244.

434 Edwards, D. P., and G. L. Francis (2000), Improvements to the correlated-k radiative
 435 transfer method: Application to satellite infrared sounding, *J. Geophys. Res.*,
 436 105(D14), 18135-18156, doi: 10.1029/2000JD900131.

437 de Haan, J. H., P. B. Bosma, and J. W. Hovenier (1987), The adding method for multiple
 438 scattering of polarized light, *Astron. Astrophys.*, 183, 371-391.

439 Ding, S., P. Yang, B. A. Baum, A. Heidinger, and T. Greenwald (2013), Development of
 440 a GOES-R Advanced baseline imager solar channel radiance simulator for ice
 441 cloud, *J. Appl. Meteor. Clim.*, 52, 872-888.

442 Dubuisson, P., J. C. Buriez, and Y. Fouquart (1996), High spectral resolution solar radiative
 443 transfer in absorbing and scattering media: Application to satellite simulation, *J.*
 444 *Quant. Spectrosc. Radiat. Transfer*, 55, 103-126.

445 Dubuisson, P., V. Giraud, O. Chomette, H. Chepfer, J. Pelon (2005), Fast radiative transfer
 446 modeling for infrared imaging radiometry, *J. Quant. Spectrosc. Radiat. Transfer*,
 447 95, 201-200.

448 Fu, Q., and K. N. Liou (1992), On the correlated k-distribution method for radiative transfer
 449 in nonhomogeneous atmospheres, *J. Atmos. Sci.*, 49, 2139-2156.

450 Hansen, J. E. (1971), Multiple scattering of polarized light in planetary atmospheres. Part
 451 I. the doubling method, *J. Atmos. Sci.*, 28, 120-125.

452 Garnier, A., J. Pelon, P. Dubuisson, M. Faivre, O. Chomette, N. Pascal, and D. Kratz
 453 (2012), Retrieval of cloud properties using CALIPSO Imaging Infrared
 454 Radiometer. Part I: Effective Emissivity and Optical Depth, *J. Appl. Meteor. Clim.*,
 455 51, 1407-1425.

456 Garnier, A., J. Pelon, P. Dubuisson, P. Yang, M. Faivre, O. Chomette, N. Pascal, P. Lucker,
 457 T. Murray (2013), Retrieval of Cloud Properties Using *CALIPSO* Imaging
 458 Infrared Radiometer. Part II: Effective Diameter and Ice Water Path, *J. Appl.*
 459 *Meteor. Clim.*, 52, 2582-2599.

460 Hansen, J. E., and L. D. Travis (1974), Light scattering in planetary atmospheres, *Space*
 461 *Sci. Rev.*, 16, 527-610.

462 Hillger, D., et al. (2013), First-light imagery from Suomi NPP VIIRS, *Bull. Amer. Meteor.*
 463 *Soc.*, 94, 1019-1029.

464 Hovenier, J. W. (1969), Symmetry Relationships for Scattering of Polarized Light in a Slab
 465 of Randomly Oriented Particles, *J. Atmos. Sci.*, 26, 488–499.

466 Hu, Y. X., B. Wielicki, B. Lin, G. Gibson, S. C. Tsay, K. Stamnes, and T. Wong, 2000:
 467 delta-Fit: A fast and accurate treatment of particle scattering phase functions with
 468 weighted singular-value decomposition least-squares fitting. *J. Quant. Spectrosc.*
 469 *Radiat. Transfer*, **65**, 681-690.

470 Kratz, D. P. (1995), The correlated *k*-distribution technique as applied to the AVHRR
 471 channels, *J. Quant. Spectrosc. Radiat. Transfer*, 53, 501-517.

472 Lacis, A. A., and V. Oinas (1991), A description of the correlated *k* distribution method for
 473 modeling nongray gaseous absorption, thermal emission, and multiple scattering in
 474 vertically inhomogeneous atmospheres, *J. Geophys. Res.*, 96 (D5), 9027-9063.

475 Lewis, J. M., D. W. Martin, R. M. Rabin, and H. Moosmüller (2010), Suomi: pragmatic
 476 visionary, *Bull. Amer. Meteor. Soc.*, 91, 559-577.

477 Lee, E. L., S. D. Miller, and F. J. Turk (2010), The NPOESS VIIRS day/night visible
 478 sensor, *Bull. Amer. Meteor. Soc.*, 87, 191-199.

479 Liou, K. N. (1973), A numerical experiment on Chandrasekhar's discrete-ordinate method
 480 for radiative transfer: application to cloudy and hazy atmospheres, *J. Atmos. Sci.*,
 481 30, 1303-1326.

482 Liu, X., W. L. Smith, D. K. Zhou, and A. Larar (2006), Principal component-based
 483 radiative transfer model for hyperspectral sensors, *Appl. Opt.*, 45, 201-209.

484 Liu, X., D. X. Zhou, A. M. Larar, W. L. Smith, P. Schluesel, S. M. Newman, J. P. Taylor,
 485 and W. Wu (2009), Retrieval of atmospheric profiles and cloud properties from
 486 IASI spectra using super-channels, *Atmos. Chem. Phys.*, 9, 9121-9142.

487 Meador, W. E., and W. R. Weaver (1980), Two-stream approximations to radiative transfer
 488 in planetary atmosphere: a unified description of existing methods and a new
 489 improvement, *J. Atmos. Sci.*, 37, 630-643.

490 Mie, G. (1908), Beiträge zur optic trüber medien, speziell kolloidaler metallösungen, *Ann.*
 491 *Phys.* 330, 377-445.

492 Moncet, J. L., G. Uymin, A. E. Lipton, and H. E. Snell (2008), Infrared radiance modeling
 493 by optimal spectral sampling, *J. Atmos. Sci.*, 65, 3917-3934.

494 Natraj, V., and R. J. Spurr (2007), A faster linearized pseudo-spherical two orders of
 495 scattering model to account for polarization in vertically inhomogeneous
 496 scattering-absorbing media, *J. Quant. Spectrosc. Radiat. Transfer*, 107, 263-293.

497 Rienecker, M. M., et al. (2008), The GEOS-5 data assimilation system - Documentation of
 498 versions 5.0.1, 5.1.0, and 5.2.0, *NASA Tech. Memo.*, TM-2008, 27 pp.

499 Robert, E. R., J. E. A. Selby, and L. M. Biberman (1976), Infrared continuum absorption
 500 by atmospheric water vapor in the 8-12 μm window, *Appl. Opt.*, 15, 2085-2090.

501 Rothman, L. S. et al. (2008), The HITRAN 2008 molecular spectroscopic database, *J.*
 502 *Quant. Spectrosc. Radiat. Transfer*, 110, 533-572.

503 Shi, G., N. Xu, B. A. Wang, T. Dai, and J. Q. Zhao (2009), An improved treatment of
 504 overlapping absorption bands based on the correlated k distribution model for
 505 thermal infrared radiative transfer calculations, *J. Quant. Spectrosc. Radiat.*
 506 *Transfer*, 110, 435-451.

507 Stamnes, K., S. C. Tsay, W. Wiscombe and K. Jayaweera (1988), Numerically stable
 508 algorithm for discrete-ordinate-method radiative transfer in multiple scattering and
 509 emitting layered media, *Appl. Opt.*, 27, 2502-2509.

510 Thomas, G. E. and K. Stamnes (1999), *Radiative Transfer in the Atmosphere and Ocean*,
 511 Cambridge University Press, New York.

512 Twomey, S., H. Jacobowitz, and H. B. Howell (1966), Matrix methods for multiple-
 513 scattering problems, *J. Atmos. Sci.*, 23, 289-296.

514 Wang, C., P. Yang, B. A. Baum, S. Platnick, A. K. Heidinger, Y. Hu, and R. E. Holz
 515 (2010), Retrieval of ice cloud optical thickness and effective particle size using a
 516 fast radiative transfer model, *J. Appl. Meteor. Clim.*, 50, 2283-2297.

517 Wang, C., P. Yang, S. L. Nasiri, S. Platnick, B. A. Baum, and A. K. Heidinger, X. Liu
 518 (2013), A fast radiative transfer model for visible through shortwave infrared
 519 spectral reflectance's in clear and cloudy atmospheres, *J. Quant. Spectrosc. Radiat.*
 520 *Transfer*, 116, 122-131.

521 Wang, C., P. Yang, S. Platnick, A. K. Heidinger, B. A. Baum T. Greenwald, Z. Zhang, and
 522 R. E. Holz (2013), Retrieval of ice cloud properties from AIRS and MODIS

523 observations based on a fast high-spectral-resolution radiative transfer model, *J.*
 524 *Appl. Meteor. Clim.*, 52, 710-726.
 525 Weisz, E., J. Li, J. Li, D. K. Zhou, H.-L. Huang, M. D. Goldberg, and P. Yang, 2007, Cloudy
 526 sounding and cloud-top height retrieval from AIRS alone single field-of-view
 527 radiance measurements *Geophys. Res. Letter* 34, L12802, doi:
 528 10.1029/2007GL030219.
 529 Yang, P., L. Bi, B. A. Baum, K. N. Liou, G. W. Kattawar, M. I. Mishchenko, and B. Cole
 530 (2013), Spectrally consistent scattering, absorption, and polarization properties of
 531 atmospheric ice crystals at wavelengths from 0.2 to 100 μm , *J. Atmos. Sci.*, 70, 330-
 532 347.

533

534 **TABLE 1.** CKD model parameters for the VIIRS channels.

VIIRS Channels	Central Wavelength (μm)	Wavelength Range (μm)	Gas Considered	Number of g values
M1	0.412	0.402-0.422	H ₂ O	4
M2	0.445	0.436-0.454	H ₂ O	4
M3	0.488	0.478-0.488	H ₂ O	16
M4	0.555	0.545-0.565	H ₂ O	4
M5	0.672	0.662-0.682	H ₂ O, O ₂ , O ₃	8
M6	0.746	0.739-0.754	H ₂ O, O ₂	8
M7	0.865	0.846-0.885	H ₂ O, O ₂	8
M8	1.240	1.23-1.24	H ₂ O, O ₂ , CO ₂	8
M9	1.378	1.371-1.386	H ₂ O	12
M10	1.61	1.58-1.64	H ₂ O, CO ₂ , CH ₄	4
M11	2.25	2.23-2.28	CH ₄ , H ₂ O, N ₂ O	4
M12	3.7	3.61-3.79	H ₂ O, CH ₄ , O ₃	4
M13	4.05	3.97-4.13	CO ₂ , H ₂ O, N ₂ O	16
M14	8.55	8.4-8.7	H ₂ O, N ₂ O, O ₃ , cont.	8
M15	10.763	10.26-11.26	H ₂ O, CO ₂ , O ₃ , cont.	4
M16	12.013	11.54-12.49	H ₂ O, CO ₂ , O ₃ , cont.	8
I1	0.64	0.60-0.68	H ₂ O, O ₂	4
I2	0.865	0.85-0.88	H ₂ O, O ₂	8
I3	1.61	1.58-1.64	H ₂ O, CO ₂ , CH ₄	4
I4	3.74	3.55-3.93	H ₂ O, N ₂ O, CH ₄	4
I5	11.45	10.5-12.4	H ₂ O, CO ₂ , O ₃ , cont.	16

535

536

537

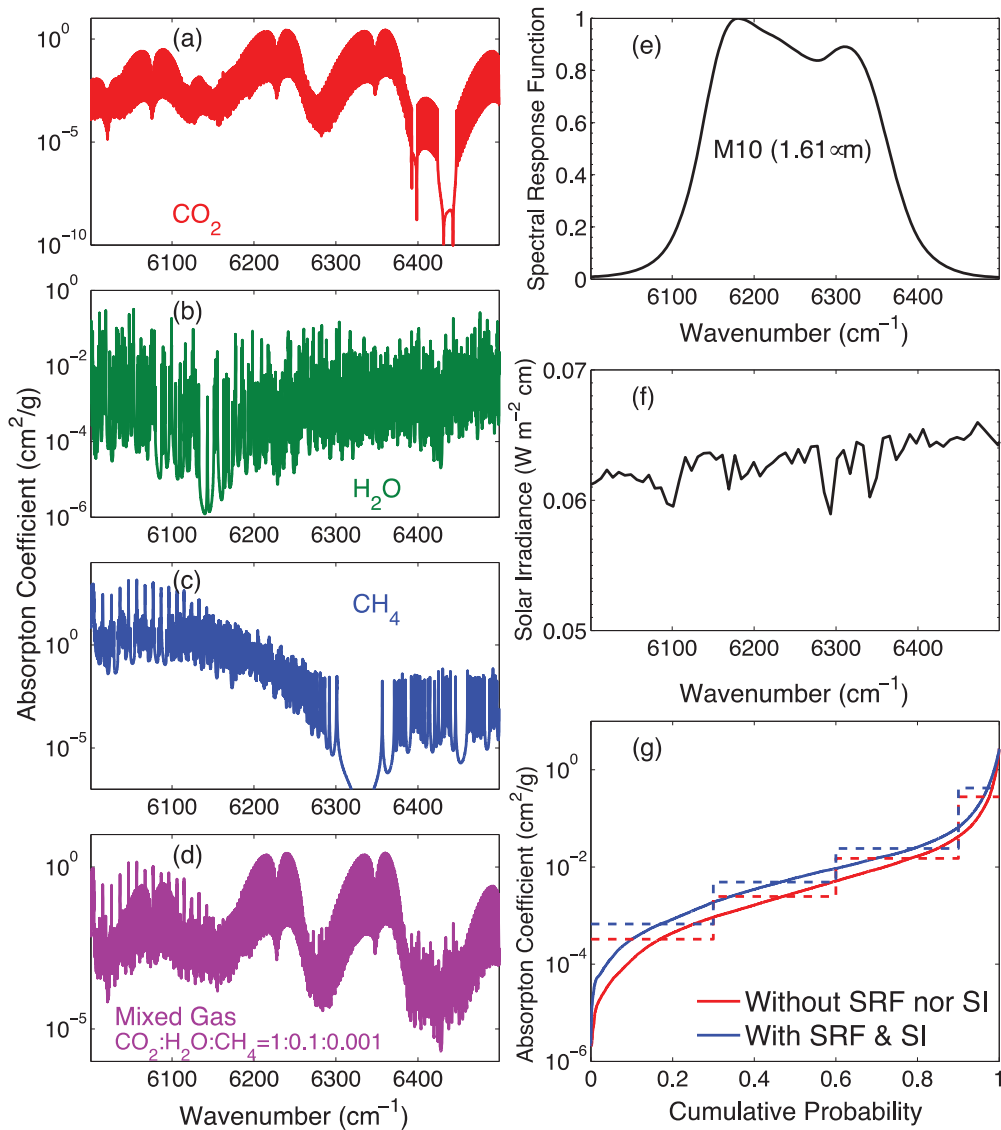


FIG. 1. Example of the treatment of overlap absorption lines, spectral response function (SRF), and solar irradiance (SI) based on the CKD algorithm for the VIIRS 1.61- μm channel. (a)-(c) Absorption coefficient as a function of wavenumber for H_2O , CO_2 , and CH_4 . (d) Absorption coefficient for a mixed case with the ratio of the three gases being 1:0.1:0.001. (e) Spectral response function. (f) Solar irradiance at the top of atmosphere. (g) Absorption coefficient as a function of cumulative probability for the mixed gas with and without the inclusion of the spectral response function and solar irradiance.

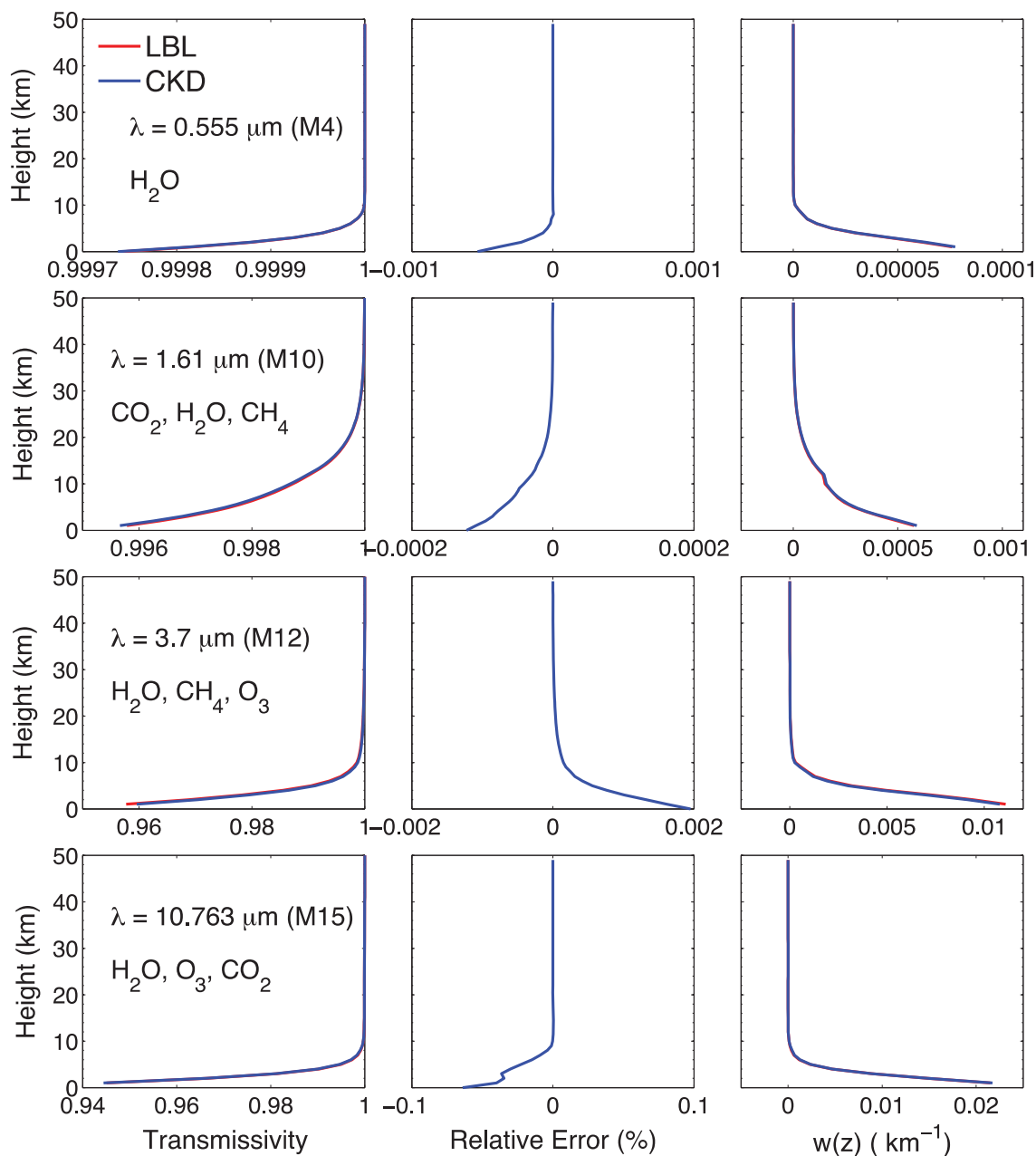


FIG. 2. Band-averaged transmissivity (left) calculated from the LBLRTM and CKD models for VIIRS 0.555-, 1.61-, 3.7-, and 10.763- μm channels. Corresponding relative errors (middle) and weight function (right) profiles of the CKD models. The U.S. standard atmospheric profile is used in the calculations.

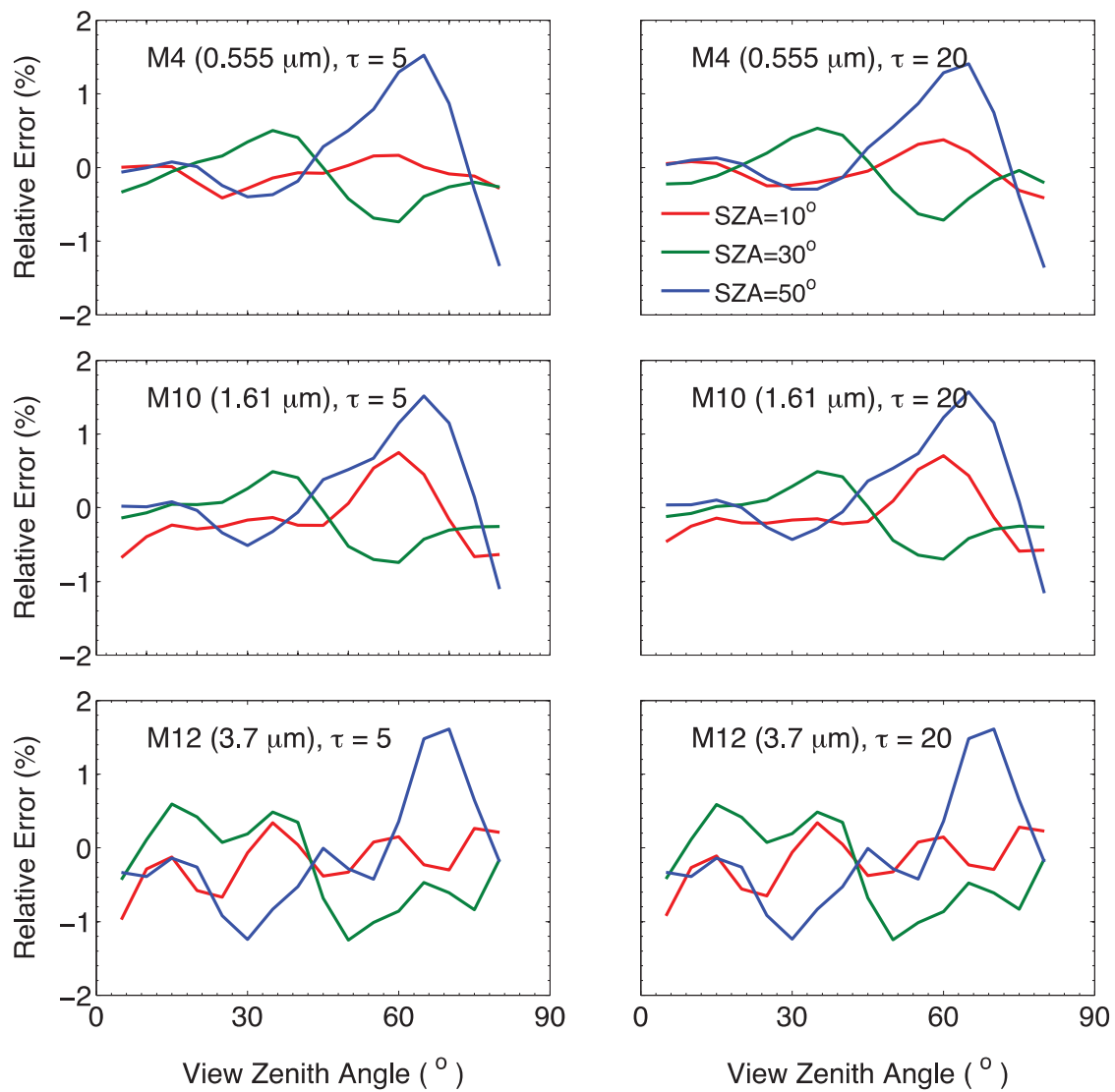


FIG. 3. Relative errors of TOA reflectance at M4 (0.555 μm), M10 (1.61 μm), and M12 (3.7 μm) channels by the VIIRS simulator in comparison with the benchmark model.

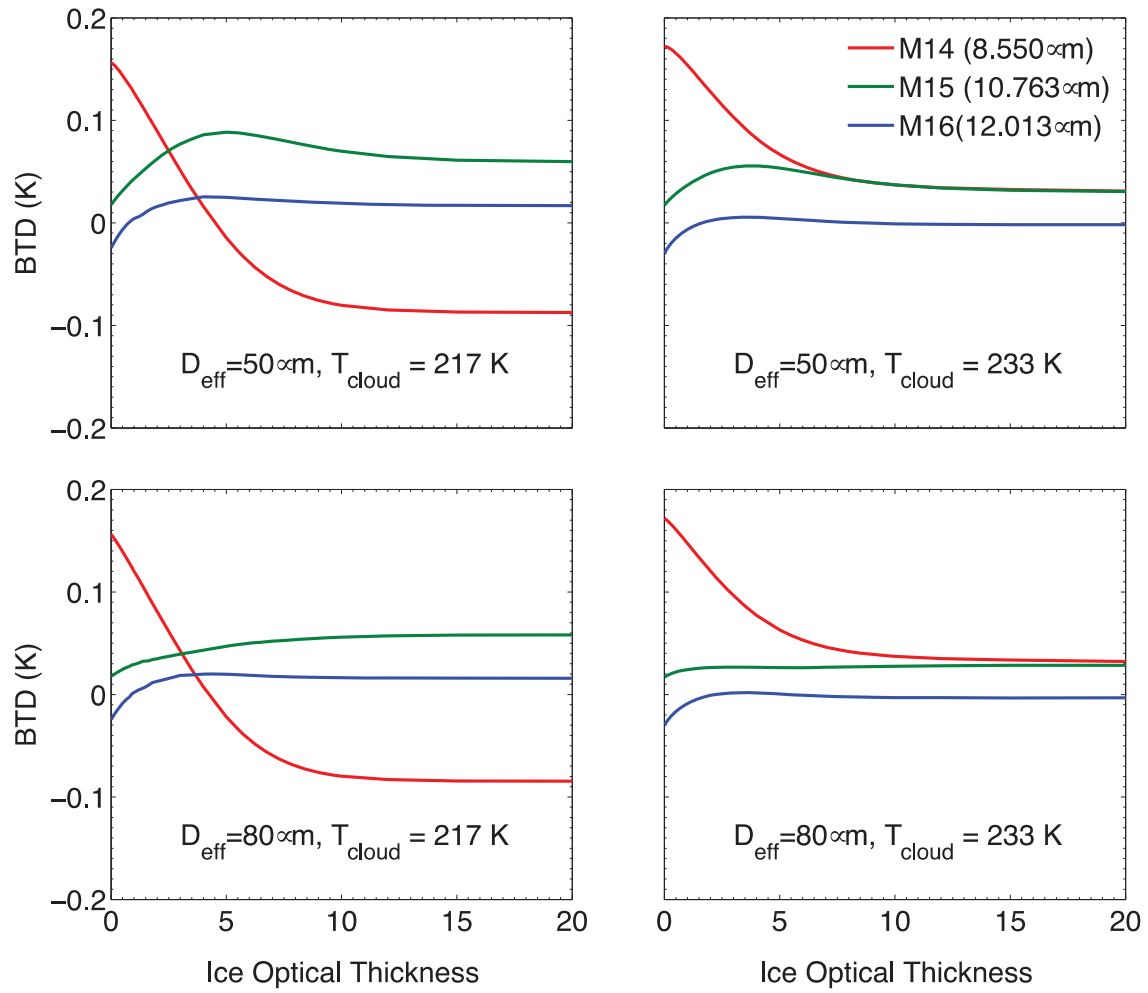


FIG. 4. Brightness temperature difference (CKD+FRTM – LBL+DISORT) as a function of ice optical thickness for a viewing zenith angle of 20° at three VIIRS infrared channels (8.55-, 10.763-, and 12.013- μm).

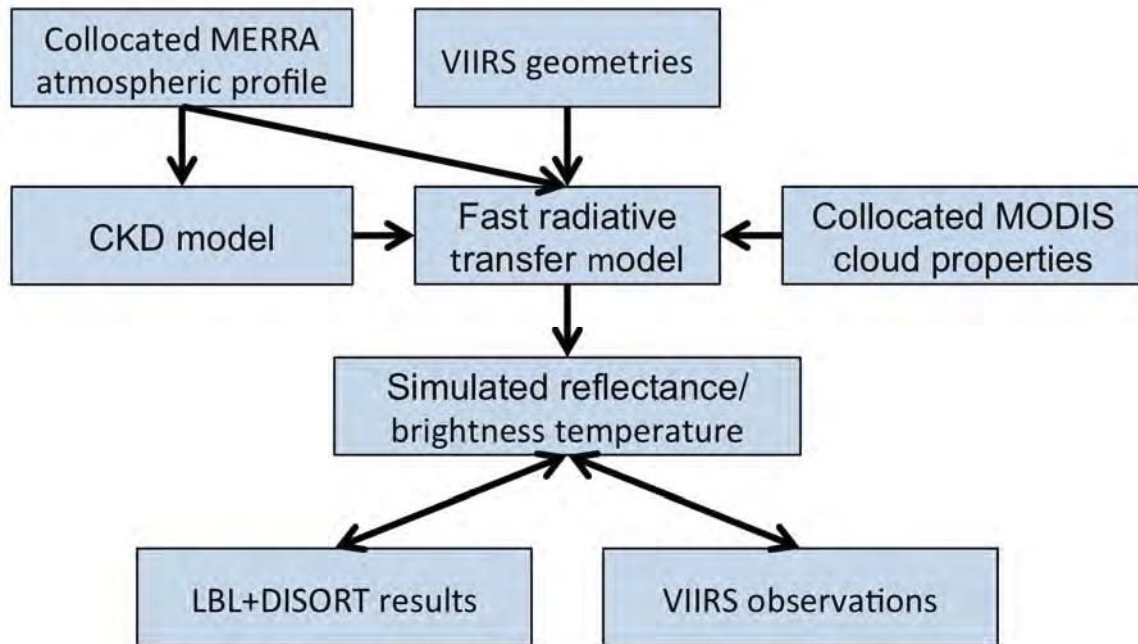


FIG. 5. Flowchart outlining the fast VIIRS radiance simulator using the collocated MERRA atmospheric profile and MODIS retrieved ice cloud thickness and effective particle size.

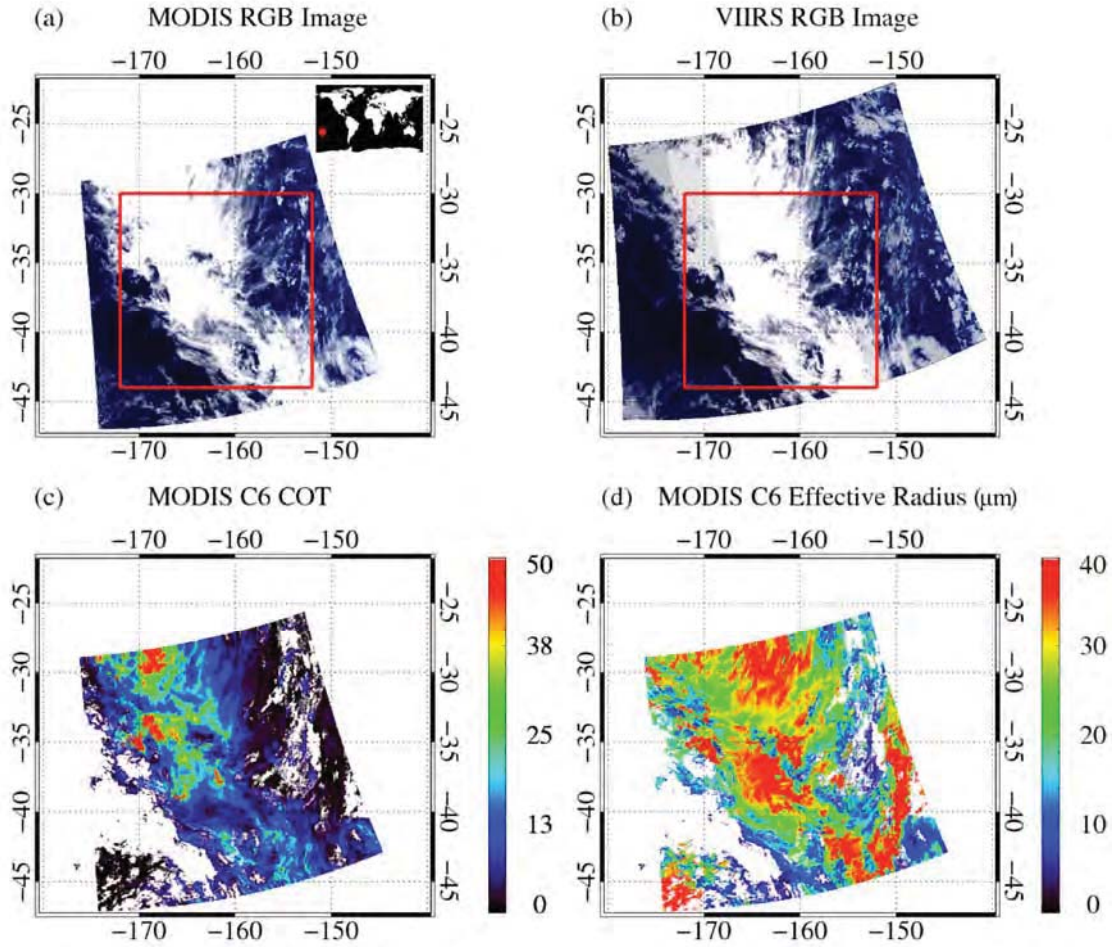


FIG. 6. (a) MODIS RGB image for a granule on 3 January 2014 at 0:45 UTC taken over the South Pacific Ocean. (b) RGB image of the corresponding VIIRS granules from 00:38:47.4 to 00:41:38.2 UTC of the same day. (c) and (d) are the MODIS Collection 6 cloud optical thickness and particle effective radius of ice clouds.

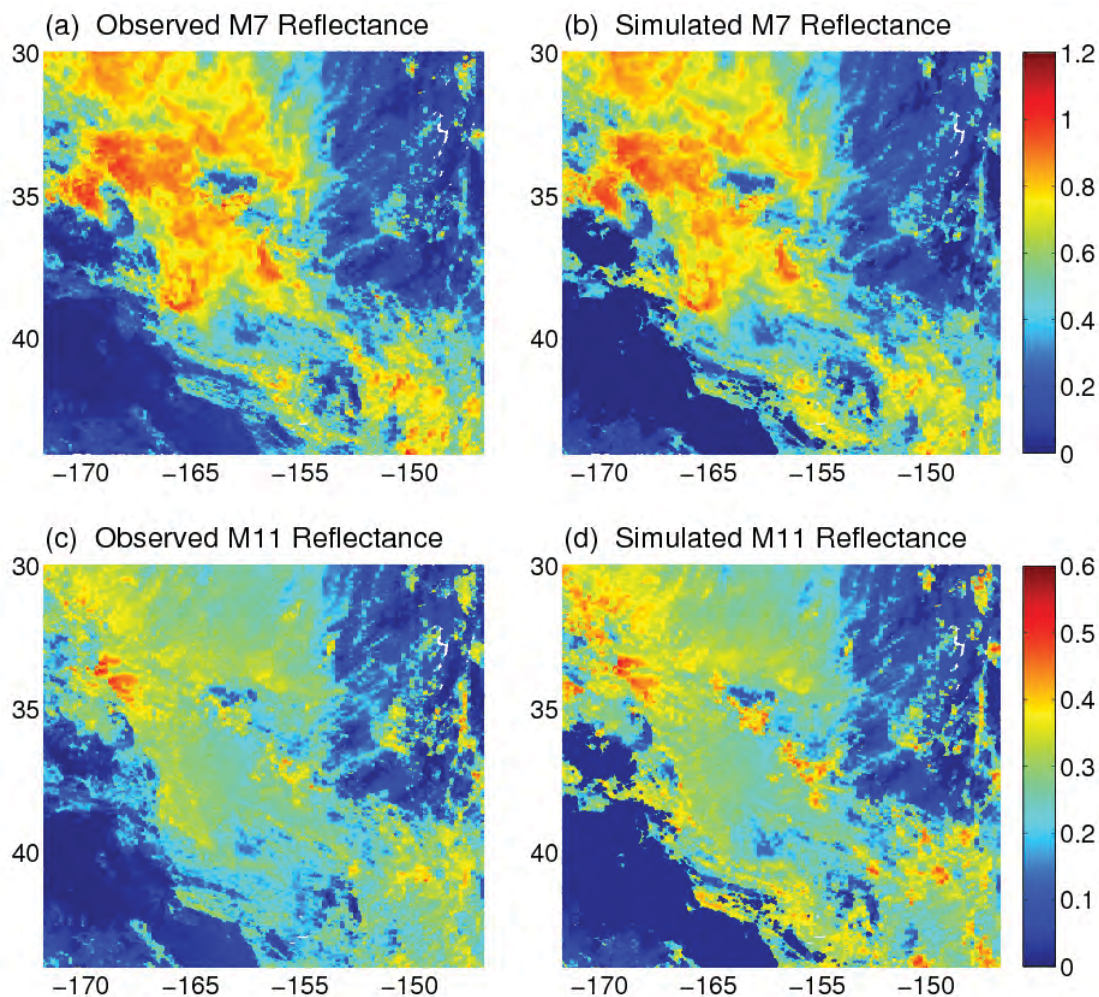


FIG. 7. Comparison between the observed (left panels) and simulated (right panels) reflectances at the VIIRS M7 (0.865 μm) and M11 (2.25 μm) channels.

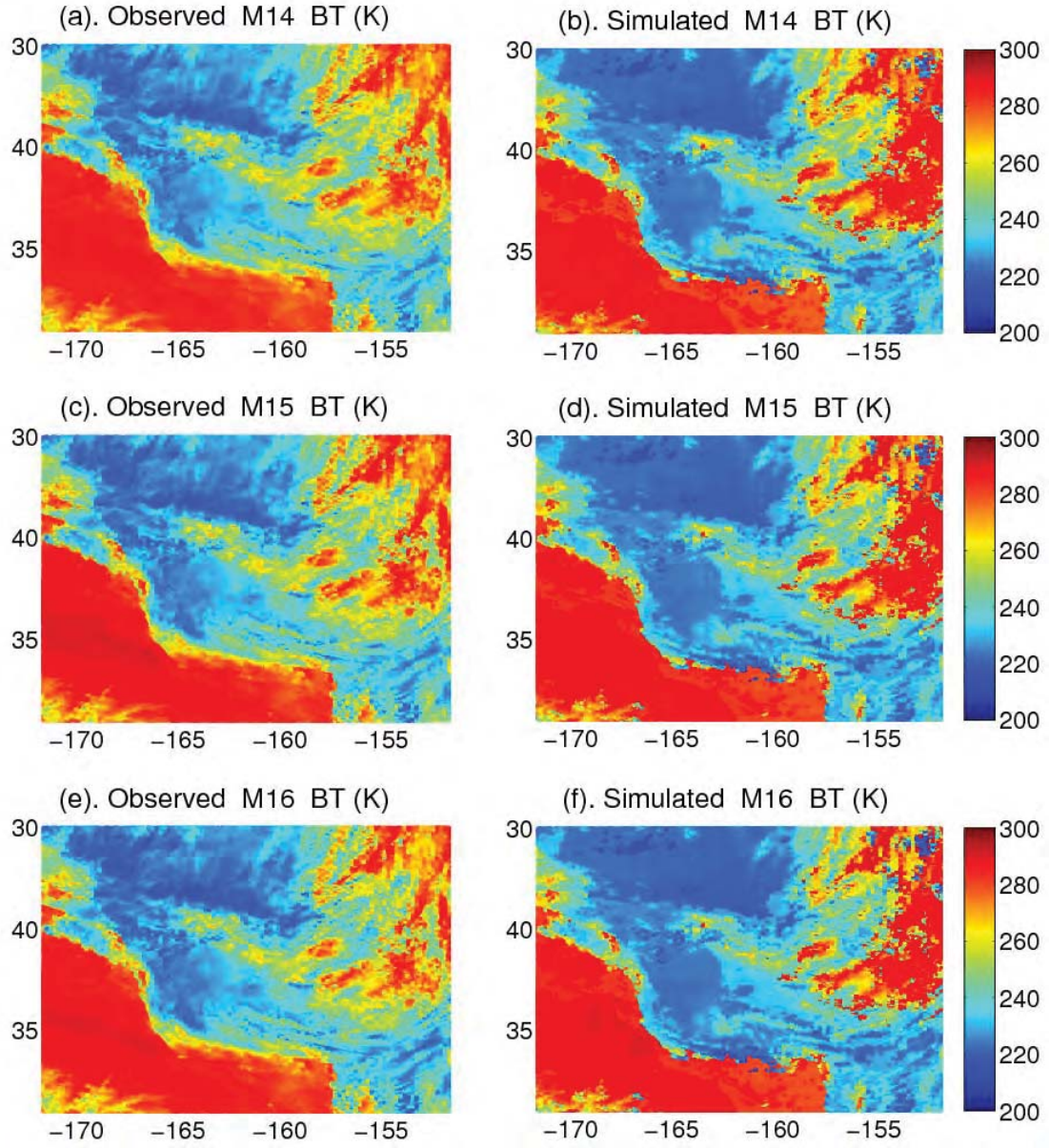


FIG. 8. Comparison between the observed (left panels) and simulated (right panels) brightness temperatures at the VIIRS M14 (8.55 μm), M15 (10.763 μm), and M11 (12.013 μm) channels.